water

MDPI

Article

A Preliminary Study of the Seepage Hammer Effect and Its Impacts on the Stability of Layered Infinite Slope

Wei-Lin Lee [1,*], Yih-Chin Tai [2], Chjeng-Lun Shieh [2] and Chih-Wei Lu [3]

1 National Science and Technology Center for Disaster Reduction, New Taipei City 23143, Taiwan
2 Department of Hydraulic and Ocean Engineering, National Cheng Kung University, Tainan 70403, Taiwan; yctai@mail.ncku.edu.tw (Y.-C.T.); shieh@dprc.ncku.edu.tw (C.-L.S.)
3 Department of Civil and Construction Engineering, National Taiwan University of Science and Technology, Taipei 106335, Taiwan; cwlu@mail.ntust.edu.tw
* Correspondence: glaciallife@gmail.com; Tel.: +886-988-567-489

Abstract: A rapid change in the pore water pressure of unsaturated soil due to a wetting front is a crucial factor and may result in instabilities in layered slopes. This study presents preliminary research on such a change, which we define as the seepage hammer effect. Vertical infiltration with multiple soil layers by column test was implemented to investigate the mechanism of the seepage hammer effect and distinguish it from the well-known Lisse effect and reverse Wieringermeer effect. A two-phase flow model was utilized to understand the evolutions of pore water/air pressure and volumetric water content, and its result evolved into a layered infinite slope stability analysis. Thus, the impacts of the seepage hammer effect on slope stability can be analyzed. This study found that the seepage hammer effect was triggered when the wetting front reached the interface of multiple layers and impermeable layers, and the rising speed of pore water pressure was proportional to the air venting capacity of soil. Slope stability analysis showed that the safety factor may decline suddenly because of the seepage hammer effect. Its relationship with the factor of safety and the sliding velocity is proportional. The detection of the seepage hammer effect could be a potential application of the study of fast-moving landslides.

Keywords: column test; two-phase flow model; seepage hammer effect

check for updates

Citation: Lee, W.-L.; Tai, Y.-C.; Shieh, C.-L.; Lu, C.-W. A Preliminary Study of the Seepage Hammer Effect and Its Impacts on the Stability of Layered Infinite Slope. *Water* **2023**, *15*, 1832. https://doi.org/10.3390/w15101832

Academic Editor: Roberto Greco

Received: 16 March 2023
Revised: 19 April 2023
Accepted: 10 May 2023
Published: 11 May 2023

1. Introduction

Rainfall-induced landslides are very common and a particularly problematic topic in mountainous countries [1–4]. The relation between the occurrence of landslides and rainfall conditions has been researched over the past 40 years [5]. Rainfall infiltration results in a change in pore water/air pressure against geological conditions, which subsequently weakens the shear strength of soils [2,4,6–13]. Thus, changes in pore water/air pressure are a critical factor that contributes to landslides. Studies on the effects of rainfall on unsaturated soil in laboratory and field conditions using pore pressure measuring devices have been conducted by other researchers [5,6,11,13–18]. Despite abundant field and laboratory data, many uncertainties remain with regard to the relation with pore water/air pressure change and rainfall infiltration.

Changes in the pore water pressure due to rainfall water are complex and have been a subject of concern for a long time. Rahardjo et al. (2005) indicated that the relation between the increase in pore water pressure and the rainfall amount is not always proportional [19]. Under relatively dry conditions (low volumetric water content, high suction), the pore water pressure decreases due to the developing capillary fringe, which is the well-known Wieringermeer effect that was first recorded by Hooghoudt (1952) [20]. After a small amount of rainfall, the pore water pressure exhibits a larger rise due to the water released from the capillary fringe; this condition is called the reverse Wieringermeer effect [12].

Then, the increase in pore water pressure is proportional to the rainfall amount until the cumulative rainfall exceeds the maximum water storage capacity of the soil layer [19]. Under excess rainfall, large and fast-rising pore water pressure may be observed [6,7,13,21–24]. If interstitial air can leak out of the soil layer freely, then high-intensity rainfall leads to the development of a wetting front with fully saturated conditions, and a suddenly ascending pore water pressure is triggered when the wetting front reaches the phreatic surface or impermeable layer [6,13,21,24]. If the interstitial air is entrapped by the infiltrated water, then an increase in pore water pressure is caused by the compression of air before the wetting front reaches the phreatic surface or impermeable layer; this phenomenon is the well-known Lisse effect [7,22,23]. Despite the well-known Wieringermeer effect and the Lisse effect, the large and fast increase in pore water pressure that results from the wetting front reaching the groundwater level and impermeable layer is rarely investigated. This study calls this phenomenon the seepage hammer effect, which is investigated in this work.

Research on the pore water pressure change in unsaturated soil has been conducted in the laboratory and through numerical modeling. In laboratory studies, 1D vertical infiltration by column test was implemented to investigate the evolutions of pore water/air pressure and volumetric water content [6,11,13,14]. Some researchers implemented laboratory tests by using 2D sandbox and 2D flume tests to investigate its relationship with soil properties and slope stability [25–28]. In numerical modeling, a single-phase flow model based on the Richards equation was utilized widely to simulate the unsaturated flow in porous media [5,15]. The change in pore water pressure might be affected by the interstitial air, i.e., the Lisse effect, which is why the two-phase flow model was developed to simulate the dynamic behavior of pore air and its impacts on the pore water pressure [6,11,12,18,24,29]. To investigate the impacts of changes in pore water/air pressure on the slope stability, the limit equilibrium method evolved in the single-/two-phase flow model [18,30,31]. The 1D slope stability analysis was widely simplified to applied infinite/finite slope theory [8,10]. This study presents preliminary research on the investigation of the seepage hammer effect considered in 1D situations. Hence, a vertical infiltration with multiple soil layers by column test was implemented, and two-phase flow model and infinite slope theory were utilized to simulate the evolutions of pore water/air pressure and its impacts on the slope stability.

This paper focuses on the seepage hammer effect, in which intense rainfall results in a sudden rise in pore water pressure at the interface of multiple layers or impermeable layers. A schematic concept of the seepage hammer effect is proposed in order to illustrate its mechanism in Section 2. In Section 3, the installation of vertical infiltration with multiple soil layers by the column test is introduced, and findings from experiments are discussed. The governing equations of the two-phase flow model, the numerical implementation (material parameters, initial condition, boundary condition, and verification), and the understanding from the numerical results are introduced in Section 4. To explore the impacts on the slope stability, infinite slope theory for unsaturated flow is introduced and its potential application on the landslide is discussed in Section 5. The conclusion of this study is given in Section 6.

2. Concept of Seepage Hammer Effect

The concept proposed in the schematic, as shown in Figure 1, was used to illustrate the phenomenon of the seepage hammer effect. When infiltration is caused by heavy rainfall (T_1), if the infiltrated water is not affected by pore air, then a piston-shaped wetting front can develop, as shown in Figure 1A [6,11,13,14]. The pore water pressure below the phreatic surface can maintain a steady state until the wetting front reaches the water table, as shown in Figure 1B. After time T_2, the pore water pressure jumps suddenly due to infiltrated water, and the increased pressure head (Δh) approximates the developing length of the wetting front (h), as shown in Figure 1C. This phenomenon is different from the Lisse effect, in which the rising pore water pressure is due to interstitial air compression [7]. It is also not the same as the reverse Wieringermeer effect, in which the change in pore water pressure

is dominated by the thickness of the capillary fringe [12]. The triggering mechanism of rapid rising pore water pressure is different and rarely discussed; thus, this phenomenon is investigated in this study and named as the seepage hammer effect.

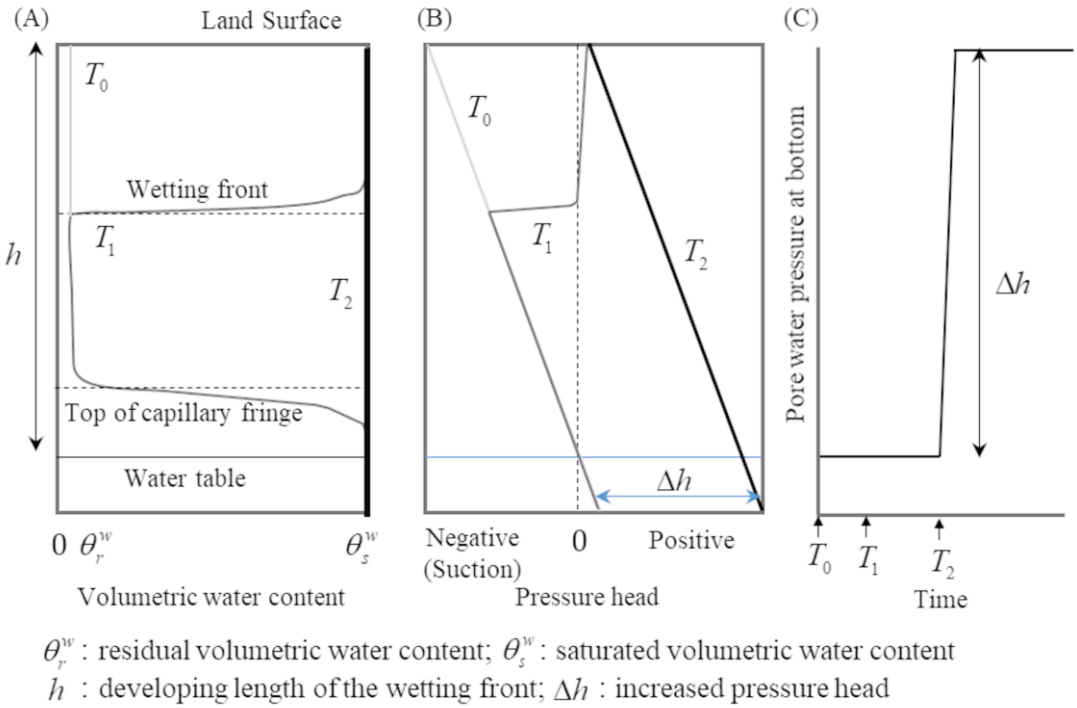

Figure 1. Sketch showing concept of the seepage hammer effect, where T_0 indicates the initial state, T_1 indicates the development of the wetting front, and T_2 indicates that the wetting front reached the water table. (**A**) Volumetric water content profile in column undergoing infiltration. (**B**) Pressure head profile; dashed vertical line—zero pressure head or atmospheric pressure. (**C**) Evolution of pressure head at the bottom. The seepage hammer effect indicates the suddenly rising pressure head due to infiltration.

3. Column Test

3.1. Column Test and Experimental Installation

To understand the seepage hammer effect, experiments of vertical infiltration in a soil column with multiple layers were implemented to investigate the evolution of pore water pressure at the bottom of the column. A sketch of the experimental installation is depicted in Figure 2A. A transparent acrylic cylinder with an inner diameter of 0.15 m and 0.95 m in height was used to set up the soil column. At the top side of the soil column, a ponding condition was considered. A constant head of water (0.04 m) was given at the top of the soil column by a water supply system. The initial groundwater in the experiment was not installed; thus, the Wieringermeer effect can be eliminated. A piezometer (cross-section diameter: 0.004 m; rate capacity: 9.8 kPa) was installed at the center of the bottom to monitor the change in pore water pressure at the bottom of the soil column. However, before the infiltrated water touched the piezometer, the pressure type of sensor was sensitive to the variation of pore air pressure. Thus, the Lisse effect can be found in the recorded data. An air valve (opening diameter 0.01 m) was installed 0.01 m above the bottom of soil column. Thus, two types of air venting were considered. In the first type (Type I, open infiltration), the air valve was open so that the interstitial air can leak outside quickly. In the second type (Type II, closed infiltration), the infiltrated water can compress the interstitial air and result in a rising pore air pressure until the interstitial air can pass through the mounted water at the top side of the soil column.

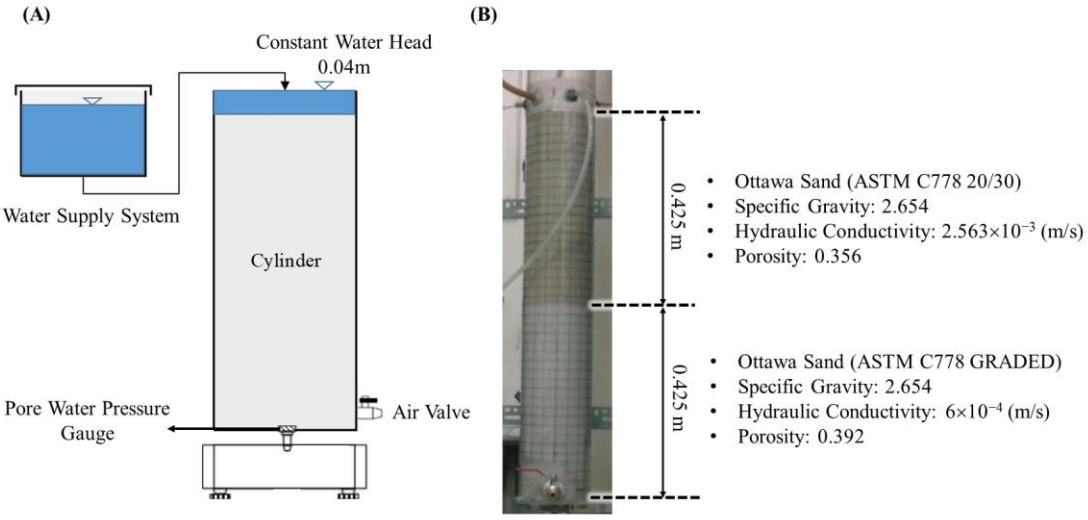

Figure 2. (**A**) Sketch of the experimental installation and (**B**) picture of the soil column.

Two layers of soil column were packed with different Ottawa sands, which were ASTM C778 20/30 (upper layer) and ASTM C778 GRADED (lower layer). Ottawa sand is poorly graded sand and uniformly distributed silica sand [32]. The main diameter of sand is 0.6 mm for the upper layer and 0.3 mm for the lower layer. The height of each layer was set to 0.425 m. A photo of the actual soil column is shown in Figure 2B. After the Ottawa sands were dried in an oven at a temperature of 110 °C ± 5 °C for 24 h, they were filled in the transparent acrylic cylinder. For homogeneous porosity, a rubber hammer was used to slightly pat the cylinder body at times during the filling process. The initial porosity of the soil column can be confirmed consistently in different experimental runs with a fixed column height and a constant weight of the sands. The material parameters of the Ottawa sands, which include specific gravity, hydraulic conductivity, and porosity, are given in Figure 2B. These parameters were confirmed in our laboratory and are close to those in Wyckoff (1936), Goetz (1971), and Lee et al. (2019) [13,33,34].

3.2. Experimental Results and Discussion

The evolutions of pore water pressure at the bottom of the soil column were recorded by a piezometer, as depicted in Figure 3. The experimental measurements of open infiltration and closed infiltration were plotted using a blue line and a brown line, respectively. With the help of experimental photos during the entire process, as shown in Figure 4, four periods of pore water pressure change can be identified by the column test. A comparison of open infiltration and closed infiltration enables further understanding of the seepage hammer effect.

For the first period P_{I}, the time began from t = 0 s to 50 s in the case of open infiltration and from t = 0 s to 60 s in the case of closed infiltration. The piezometer measured a slight rise of ca. 0.5 kPa and ca. 1.5 kPa in open infiltration and closed infiltration, respectively. At this moment, the infiltrated water was far away from the pressure sensor and did not touch the interface of the two layers (cf. Figure 4A,E). The air valve was close in $P_{\mathrm{I}}^{\text{type-II}}$. Thus, the slight rise was due to the Lisse effect [7,9,13]. However, the air venting controller was open in $P_{\mathrm{I}}^{\text{type-I}}$. Whether the Lisse effect existed in $P_{\mathrm{I}}^{\text{type-I}}$ and caused the smaller rise of pore air pressure (ca. 0.5 kPa) can be confirmed by 1D numerical study. In this period, the varying pore pressure was not caused by the seepage hammer effect but by the Lisse effect.

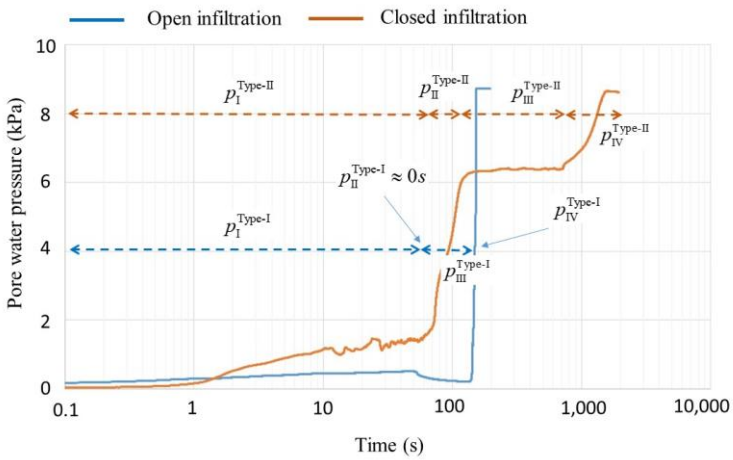

Figure 3. Evolutions of pore water pressure from the column test. The cases of open infiltration and closed infiltration are depicted using a blue line and a orangeline, respectively. P_{I} indicates the period of wetting front development in the upper layer until it reached the interface of the two layers, P_{II} indicates the period of ground water rising in the upper layer until it reached the surface of the soil column, P_{III} indicates the period of wetting front development in the lower layer until it reached the bottom of the soil column, and P_{IV} indicates the period of groundwater rising in the lower layer until it reached the interface of the two layers.

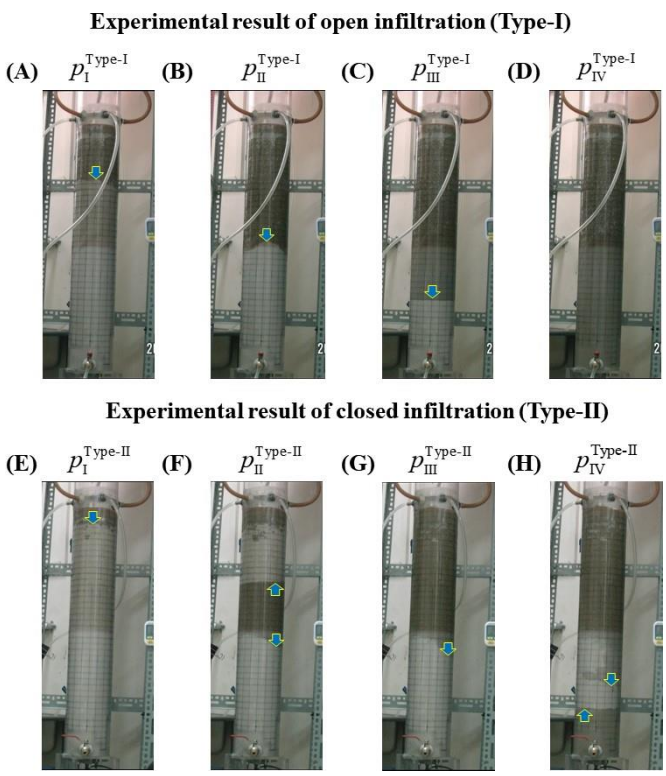

Figure 4. Experimental pictures of open infiltration (**A**–**D**) and closed infiltration (**E**–**H**), and the process can be classified with four periods. P_{I} indicates the period of wetting front development in the upper layer until it reached the interface of the two layers, P_{II} indicates the period of ground-water rising in the upper layer until it reached the surface of the soil column, P_{III} indicates the period of wetting front development in the lower layer until it reached the bottom of the soil column, and P_{IV} indicates the period of groundwater rising in the lower layer until it reached the interface of the two layers.

For the second period P_{II}, a rising pore pressure from ca. 1.5 kPa to ca. 6.1 kPa can be found in the case of closed infiltration during t = 60 s to 120 s. However, no similar situation was observed for open infiltration. According to Figure 4B,F, the infiltrated water still did not touch the piezometer, and the air venting controller was not open in the case of closed infiltration. Therefore, this study inferred that the rising pore pressure was due to air compression (Lisse effect). In the case of closed infiltration, the increasing value of pore pressure was about 4.6 kPa. After the upper layer was close to full saturation, the constant head of water (0.04 m) and the height of stored water in the upper layer (0.425 m) can contribute about 4.56 kPa pore water pressure on the interface of the two layers. Thus, these recorded data illustrated that the generated pore water pressure at the interface of the two layers can transmit to the bottom with the help of the Lisse effect. The findings imply that the infiltrated water can cause a rising pore pressure into the underground under some specific conditions of geological structures and soil properties (i.e., high permeability). In this period, the infiltrated water should cause a rising pore water pressure on the interface of the two layers, which means that the seepage hammer effect should work at that location. However, no direct measurement of pore water pressure was made on the interface. This study proves this explanation by using a 1D numerical model.

For the third period, the time began from t = 50 s to 140 s in the case of open infiltration and from t = 120 s to 750 s in the case of closed infiltration. In this stage, the infiltrated water had passed through the interface of the two layers but had not yet touched the bottom of soil column (cf. Figure 4C,G). In the case of open infiltration, the air valve was open (Type I), and the reading from the piezometer remained at a smaller value (ca. 0.2 kPa) than in $P_{I}^{\text{type-I}}$. The mechanism can be explained with the help of 1D numerical analysis late. In the case of closed infiltration, the interstitial air passed through the upper layer and the mounted water at the soil top in the form of bubbles, and so the pore pressure maintained as a fixed value [13]. As described by Horton (1941) [14], the infiltration rate corresponds to the air venting rate. Accordingly, the wetting front development in $P_{III}^{\text{type-II}}$ slowed and moved downward with a fingering pattern (cf. Figure 4G). The column test indicates that the change in pore pressure at the bottom was slight regardless of the seepage hammer effect.

In the fourth period, the pore water pressure increased significantly in the cases of Types I and II. The rising pore water pressure was triggered after the wetting front touched the bottom (cf. Figure 4D,H). This condition was caused by infiltrated water, which indicates that the seepage hammer effect occurred. In the case of open infiltration, the interval time for rising pore water pressure was about 10 s, and the change value of pore water pressure (ca. 8.7 kPa) approximated the total water head of the soil column (0.89 m). In the case of closed infiltration, the rising pore water pressure took longer than 1000 s; the pore water pressure increased slowly until it was close to the total water head of the soil column. This finding shows that the rising speed of pore water pressure was positively related to the infiltration rate and the air venting rate, thus implying that the intensity of the seepage hammer effect can be attributed to some specific conditions of soil properties (i.e., high air permeability).

In summary, first, the seepage hammer effect is triggered when the infiltrated water touches the bottom (impermeable surface). Second, with the help of the Lisse effect, the seepage hammer effect can transmit to deeper ground immediately. Third, the intensity of the seepage hammer effect is positively related to the air venting capacity of soil.

4. 1D Numerical Model

4.1. 1D Numerical Model and Numerical Implementation

To investigate the evolutions of pore water pressure profile, pore air pressure profile, and volumetric water content profile, a 1D numerical model was applied instead of experimental measurement using multiple sensors. The numerical model is a commercial software (GeoStudio by GEO-SLOPE International Ltd., Calgary, AB, Canada), and its SEEP/W and AIR/W modules were employed in this study. The simulation of the column test aimed to verify the seepage hammer effect observed in the experiment.

The numerical model based on two-phase flow was used to simulate the column test. With the assumption that the water and air exhibit immiscible flow in a porous media, these two fluids flow in the vertical direction following the generalized Darcy's law. The model equation for the water phase can be read as

$$m_w \gamma_w \frac{\partial H^w}{\partial t} = \frac{\partial}{\partial y}\left(k^w \frac{\partial H^w}{\partial y}\right) + m_w \frac{\partial p^a}{\partial t} + Q_w, \tag{1}$$

where γ_w is the unit weight of water, t is the time, y indicates the elevation, k^w is the hydraulic conductivity of water, p^a is the pore air pressure, and Q_w is the applied boundary flux. In Equation (1), the total hydraulic head is $H^w = p^w/\gamma_w + y$, p^w is the pore water pressure. The slope of the storage function is $m_w = -\partial\theta^w/\partial p_c$, in which θ^w is the volumetric water content and p_c is the suction. The suction is $p_c = p^a - p^w$. For the air phase, the model equation is expressed as

$$\left(\frac{\theta^a}{RT} + \rho_a m_w\right)\frac{\partial p^a}{\partial t} = \frac{\partial}{\partial y}\left(\frac{\rho_a k^a}{\rho_{ao} g}\frac{\partial p^a}{\partial y} + \frac{{\rho_a}^2 p^a}{\rho_{ao}}\right) - \frac{\theta^a p^a}{R}\frac{\partial}{\partial y}\left(\frac{1}{T}\right) + \rho_a m_w \gamma_w \frac{\partial H^w}{\partial t}, \tag{2}$$

where θ^a is the volumetric air content, R is the gas constant, T is the temperature, ρ_a is the density of air, ρ_{ao} is the initial density of air, k^a is the hydraulic conductivity of air, and g is the gravitational acceleration. In this study, the isothermal condition was considered. Thus, the temperature gradient in Equation (2) can be ignored.

The hydraulic conductivities for water and air are sensitive to the volumetric water content and the suction [6,11,13]. The well-known van Genuchten–Mualem model was utilized in this study. Van Genuchten (1980) [35] described the volumetric water content function for suctions as given by

$$\theta^w = \theta_r^w + \frac{\theta_s^w - \theta_r^w}{\left[1 + \left(\frac{p_c}{a}\right)^n\right]^m}, \tag{3}$$

where θ_r^w is the residual volumetric water content, and θ_s^w is the saturated volumetric water content. In Equation (3), a indicates the air entry value (unit is kPa), and three parameters (a, m, and n) can be regressed by experimental results. Thus, the change in volumetric water content against the varying suction can be estimated. The effective degree of saturation S_e can be calculated by $(\theta^w - \theta_r^w)/(\theta_s^w - \theta_r^w)$. Mualem (1976) [36] presented the hydraulic conductivities of water for S_e by

$$k^w = k_s^w {S_e}^{0.5}\left[1 - \left(1 - S_e^{\frac{n}{n-1}}\right)^{\frac{n-1}{n}}\right]^2, \tag{4}$$

and the hydraulic conductivities of water for S_e by

$$k^a = k_d^a (1 - S_e)^{0.5}\left(1 - S_e^{\frac{n}{n-1}}\right)^{\frac{2(n-1)}{n}}. \tag{5}$$

In Equations (4) and (5), k_s^w denotes the saturated hydraulic conductivity, and k_d^a is the air conductivity in the dry condition.

The configuration in the simulation was presented as shown in Figure 5. In all simulation cases, as shown in Figure 5A, the computation domain was divided into two regions: the upper region was from y = 0.425 m to y = 0.85 m, and the lower region was from y = 0 m to y = 0.425 m. The mesh size was constant with Δy = 0.01 m, and the time step was given as Δt = 1 s. For the unsaturated soil behavior, the van Genuchten formula (cf. Equation (3)) is crucial to determine the material parameters, which include residual volumetric water content θ_r^w, saturated volumetric water content θ_s^w, and fitting parameters (a, m, and n). For the two-phase flow, the Mualem formulae (cf. Equations (4) and (5)) describe the changes in water and air hydraulic conductivities against volumetric water content, in which the saturated hydraulic conductivity k_s^w and air conductivity in the dry condition k_d^a are important material parameters. In the upper region of the computational domain, Ottawa sand (ASTM C778 20/30) was assigned, and its variant parameter values have been reported [13,37]. In this study, the parameters for ASTM C778 20/30 θ_r^w = 0.016 (m^3/m^3), θ_s^w = 0.356 (m^3/m^3), a = 1.364 kPa, m = 0.89, n = 8.9, k_s^w = 2.563 × 10^{-3} (m/s), and k_d^a = 7 × 10^{-2} (m/s) were chosen as in Lee et al. (2019) [13]. For the lower region, material parameters of ASTM C778 GRADED were assigned. According to the laboratory test (cf. Figure 2B), the parameters for ASTM C778 GRADED θ_s^w = 0.392 (m^3/m^3) and k_s^w = 6 × 10^{-4} (m/s) were determined. The fitting parameters of the van Genuchten formula for ASTM C778 GRADED, in which a = 2.045 kPa, m = 0.8, and n = 5, were reported by Amankwah et al. (2021) [38]. Then, θ_r^w = 0.018 (m^3/m^3) and k_d^a = 1.5 × 10^{-5} (m/s) for ASTM C778 GRADED were given by back analysis. All parameters are listed in Table 1.

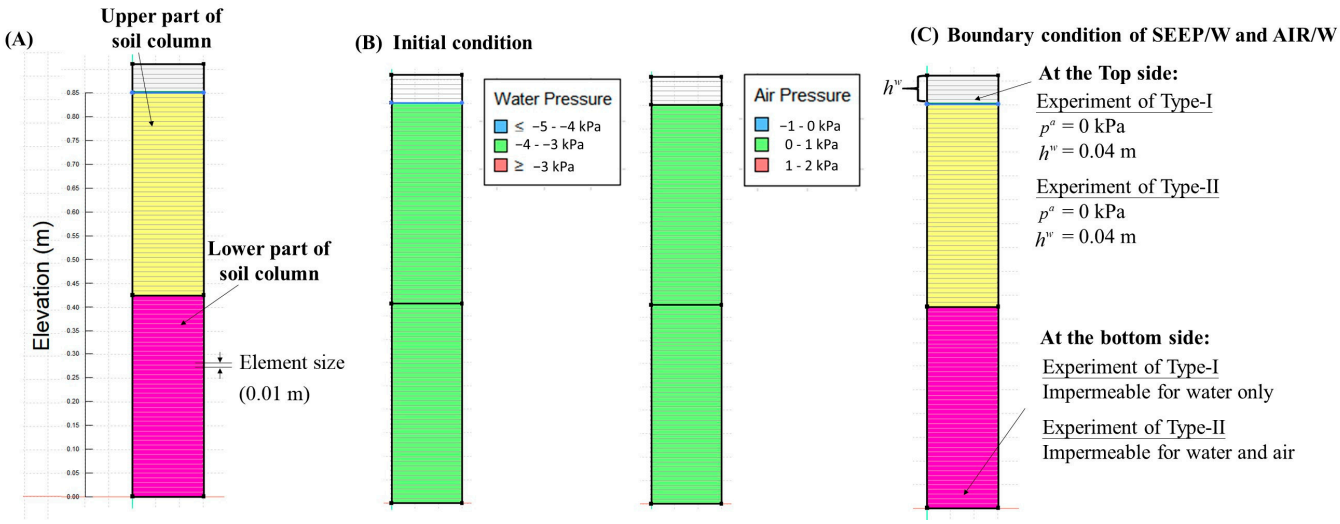

Figure 5. Configuration in simulation: (**A**) The computational domain and its mesh assignment; (**B**) initial condition of pore water and air pressure; (**C**) boundary conditions of AIR/W and SEEP/W.

Table 1. Material parameters of ASTM C778 20/30 and ASTM C778 GRADED.

Material Parameters	Upper Layer (ASTM C778 20/30)	Lower Layer (ASTM C778 GRADED)
Residual volumetric water content θ_r^w (m^3/m^3)	0.016	0.018
Saturated volumetric water content θ_s^w (m^3/m^3)	0.356	0.392
Fitting parameter a (kPa)	1.364	2.045
Fitting parameter n	8.9	5
Fitting parameter m	0.89	0.8
Saturated hydraulic conductivity k_s^w (m/s)	2.563 × 10^{-3}	6 × 10^{-4}
Air conductivity in the dry condition k_d^a (m/s)	7 × 10^{-2}	1.5 × 10^{-5}

The initial and boundary conditions were assigned as depicted in Figure 5B,C, respectively. For unsaturated soil, the capillary, transition, and residual zones can be identified based on the given fitting parameters of the van Genuchten formula [6,39]. The initial volumetric water content of soil can be given by an initial value of suction. According to the experimental installation, the Ottawa sands were filled in the transparent acrylic cylinder under dry conditions. In reference to the fitting parameters of the van Genuchten formula in Table 1, the initial pore water and air pressures were set as −4 kPa and 0 kPa in all simulations, respectively. The boundary conditions were adopted for the cases of open infiltration and closed infiltration. In all experimental cases, a constant head water was positioned at the surface of the soil column so that the boundary condition at the top was a fixed water head 0.04 m for SEEP/W and a fixed air pressure of 0 kPa for AIR/W. In the case of open infiltration, the air venting controller was kept open so that the boundary condition at the bottom was impermeable for water but permeable for air. In the case of closed infiltration, the interstitial air can leak out from the top only, so the boundary condition at the bottom was impermeable to water and air.

4.2. Simulated Results and Discussion

The employed parameter values for the simulation were verified by the pore water pressure at the bottom of the soil column. Sound agreement with the open infiltration experiment and numerical modeling was obtained. In the case of closed infiltration, the characteristics of pore water pressure in different stages can be represented in the simulation. The evolutions of measured and simulated pore water pressure change at the cylinder bottom are depicted in Figure 6.

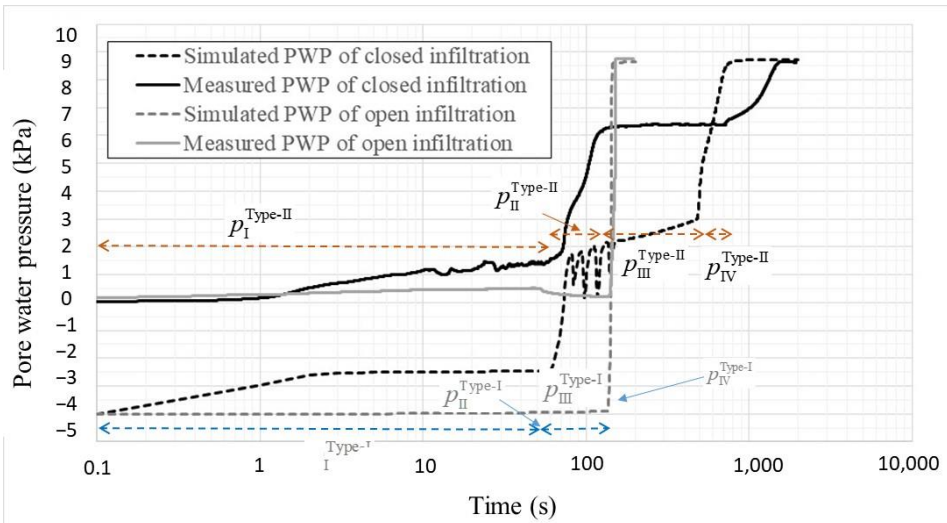

Figure 6. Evolutions of measured and simulated pore water pressure change at the cylinder bottom.

For the first period P_I, the simulated interval time of open infiltration and closed infiltration were approximate numerical results. Section 3.2 mentioned that the observed pore pressure change was not caused by seepage hammer effect but was a result of the Lisse effect. Through simulated results, as shown in Figure 7, the findings can be investigated further. From the profile of simulated saturation (θ^w/θ_s^w), as shown in Figure 7A,C, the wetting front was developed from the top due to infiltration, and the bottom of the soil column stayed dry. This finding illustrates that the infiltrated water cannot cause a rising pore water pressure at the bottom in P_I. In the case of closed infiltration, before t = 60 s, a minor rise of pore air pressure (ca. 1.5 kPa) was exhibited in the simulation due to air compression, as shown in Figure 7F. Thus, the observed slightly rising pore pressure in $P_I^{\text{type-II}}$ can be confirmed as the Lisse effect. An interesting finding from the numerical modeling was that the Lisse effect also existed in the upper layer of open infiltration with

a smaller rise of pore air pressure (ca. 1.0 kPa), as shown in Figure 7C. The boundary condition at the bottom was a permeable condition for air (cf. Figure 5), which was why the simulated pore air pressure dissipated as the interstitial air passed through the lower part of soil column (cf. Figure 7C, t = 50 s, and location range from y = 42.5 m to y = 0 m). In the column test, the pore air pressure cannot dissipate to zero as in the numerical modeling because the opening diameter of the air valve (0.01 m) is not large enough for air venting freely. This finding explains why the measured rise of pore pressure at the bottom in $P_{\mathrm{I}}^{\text{type-I}}$ was about 0.5 kPa (cf. Figure 3). Through numerical and experimental studies, this study confirmed that the varying pore pressure at the bottom in P_{I} was caused by the Lisse effect.

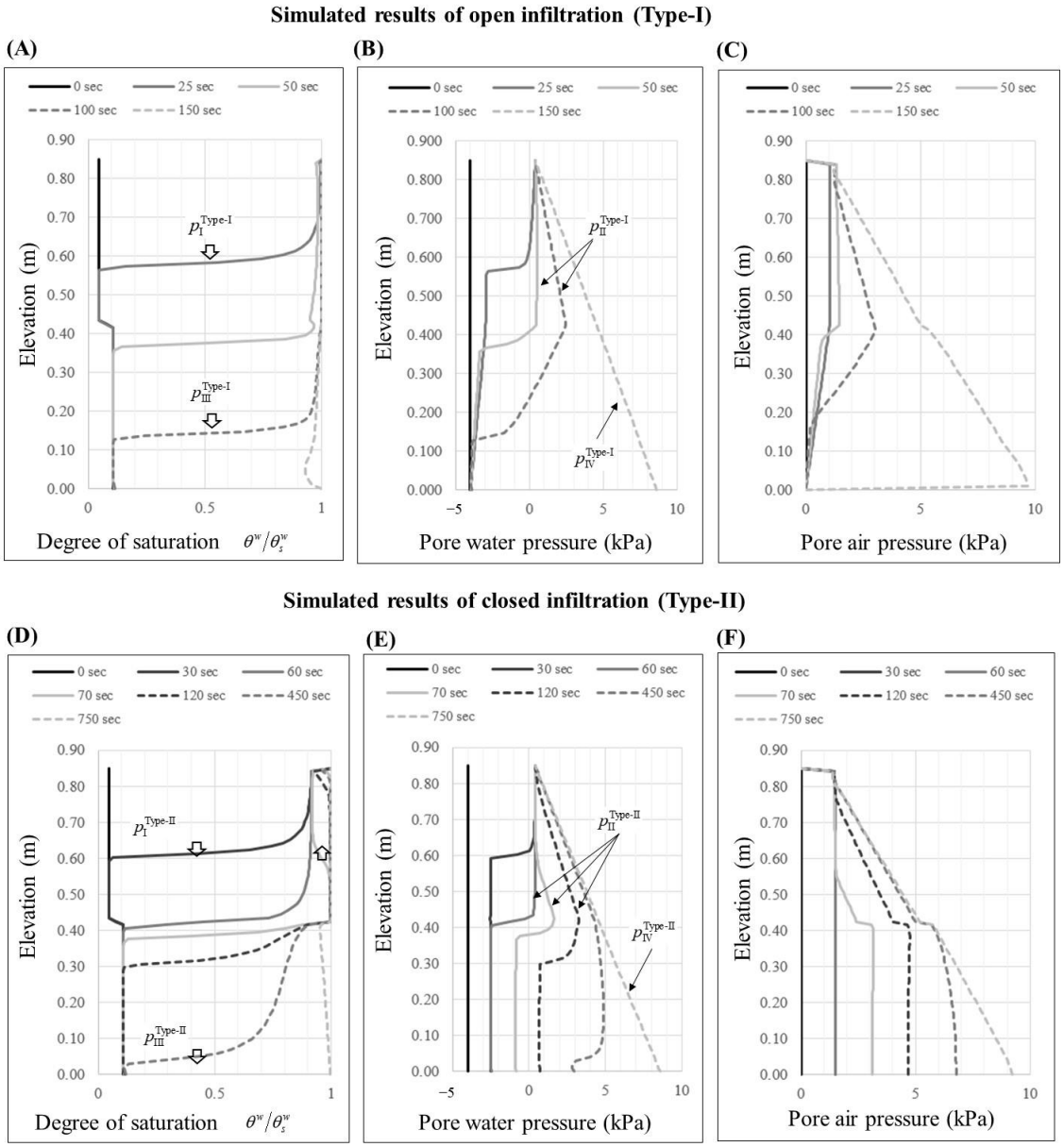

Figure 7. Simulated results of open infiltration (**A**–**C**) and closed infiltration (**D**–**F**). The arrow indicates the direction of wetting front.

For the second period P_{II}, in Section 3.2, the seepage hammer effect was triggered at the interface of the two layers, and the rising pore pressure at the bottom of closed infiltration was caused at the same time with the help of the Lisse effect. Numerical modeling showed that when the wetting front reached the interface of the two layers (cf. Figure 7A, t = 50 s, and Figure 7D, t = 60 s), the pore water pressure in the upper layer increased due to infiltrated water (Figure 7B, t = 50 s, and Figure 7E, t = 60 s to 120 s). In the case of closed infiltration, as shown in Figure 7E,F, from t = 60 s to 120 s, the increasing pore air pressure at the bottom (from ca. 1.5 kPa to ca. 4.7 kPa) approximated the rising pore water pressure at the interface of the two layers (from ca. −0.3 kPa to ca. 3.3 kPa). This finding illustrates that the infiltrated water filled the upper layer and caused the compression of interstitial air in the lower layer at the same time. Through numerical analysis, this study confirmed that the seepage hammer effect was triggered in the upper layer when the wetting front reached the interface of the two layers, and it can cause a rising pore pressure in a deeper location at the same time with the help of the Lisse effect.

For the third period P_{III}, in Section 3.2, the change in pore water pressure at the bottom was minor and the seepage hammer effect was not observed at this moment. According to the simulated results, as depicted in Figure 7A,D, the wetting front developed in the lower layer until it reached the bottom. In the case of open infiltration, as shown in Figure 7A,C, i.e., t = 100 s, where the wetting front passed through (from y = 0.85 m to y = 0.2 m), the suction ($p_c = p^a - p^w$) reduced to 0 kPa, so the simulated pore air pressure was equal to the simulated pore water pressure. The evolution of simulated pore air pressure in the lower layer varied due to the disappearance of the suction but not the air compression. Thus, in the case of open infiltration, the pore pressure at the bottom remained at a fixed value. In the case of closed infiltration, after t = 120 s, the pore air pressure in the lower layer increased in the simulation; thus, the simulated pore water pressure at the bottom increased. This result was inconsistent with the observed data. This study considered that the employed parameters of Equation (5) might not match the column test well. How to provide suitable parameters for pore air-related formula should be investigated further. Through numerical and experimental studies, in P_{III}, this study confirmed that the varying pore pressure at the bottom was not a result of the seepage hammer effect.

For the last period P_{IV}, in Section 3.2, the rising pore water pressure at the bottom was triggered by infiltrated water, a phenomenon that is also called the seepage hammer effect. In the numerical modeling of open infiltration, the pore water pressure jumped suddenly as the wetting front reached the bottom (cf. Figure 7A, t = 100 s to 150 s), and the pore water pressure changed from −4 kPa to 8.6 kPa (cf. Figure 7B, t = 100 s to 150 s). According to the numerical modeling of closed infiltration, the time it took for the lower layer to be filled with infiltrated water was longer than that in the case of open infiltration because the simulated air venting rate at the top became smaller. Through numerical and experimental studies, in P_{IV}, this study confirmed that the seepage hammer effect was triggered after the wetting front reached the bottom, and the rising speed of pore water pressure was a response to the infiltration rate and the air venting rate.

In sum, first, the seepage hammer effect is triggered not only as the infiltrated water touches the impermeable layer but also as the infiltrated water touches the interface of multiple layers. Second, with help of the Lisse effect, the seepage hammer effect can transmit to deeper ground immediately. Third, the intensity of the seepage hammer effect (rising speed of pore water pressure) is positively related to air venting capacity. The schematic concept of the seepage hammer effect in multiple layers is shown in Figure 8.

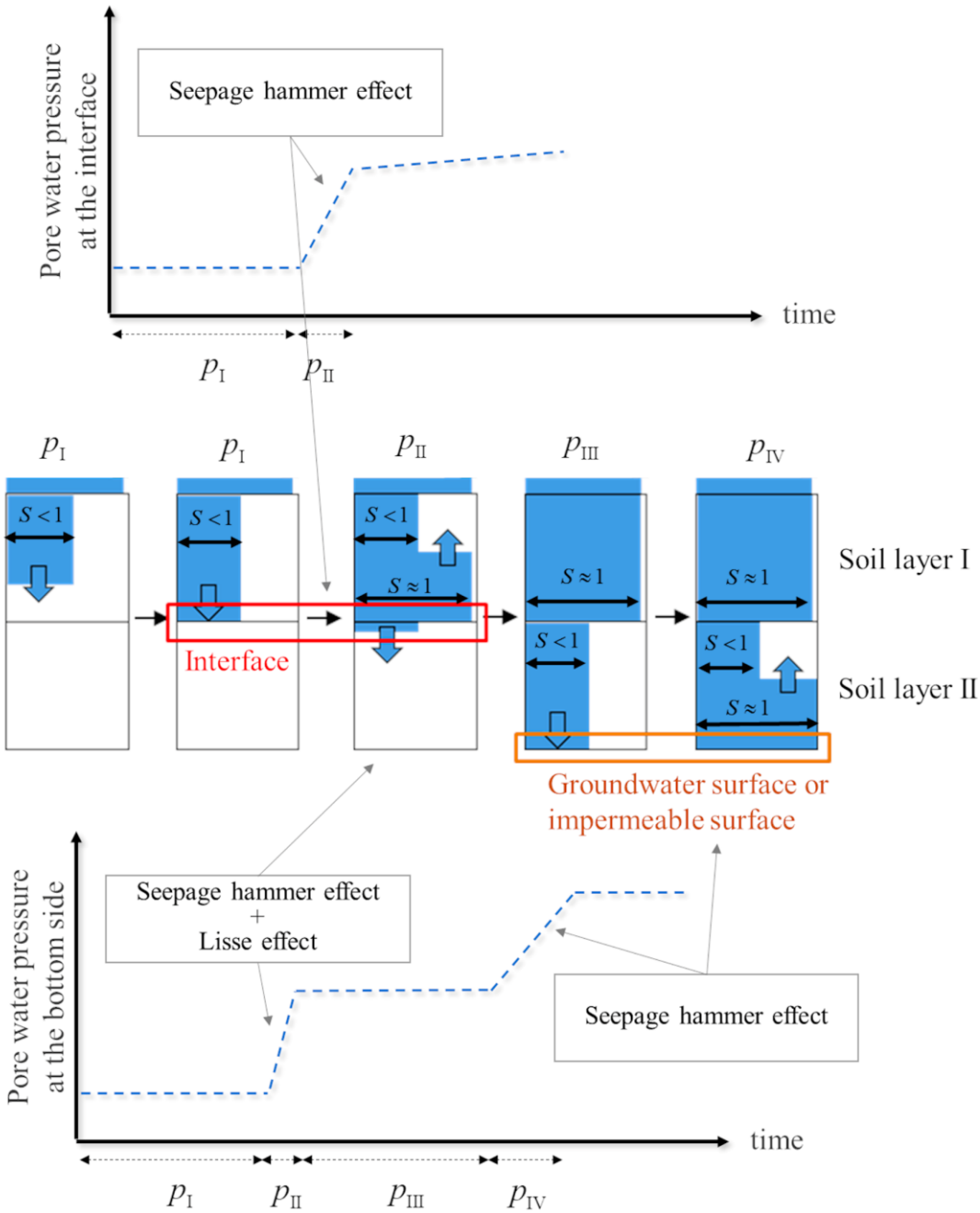

Figure 8. Schematic concept of the seepage hammer effect in multiple layers.

5. Impact of the Seepage Hammer Effect on Infinite Slope Stability

The seepage hammer effect can trigger rising pore water pressure on the interface of multiple layers or impermeable layers via infiltrated water. The varying pore water pressure can cause a change in slope stability. This subject has been researched widely in geotechnical engineering [10]. Thus, the impact of the seepage hammer effect on infinite slope stability was investigated in this preliminary study.

Under partially saturated conditions, the safety factor at any depth can be analyzed according to the infinite slope stability [8], and it reads as

$$FS(y) = \frac{2c(y)}{W(y)\sin 2\theta} + \frac{\tan\phi}{\tan\theta} + \frac{(p^a(y) + S_e(y)p_c(y))}{W(y)}(\cot\theta + \tan\theta)\tan\phi, \quad (6)$$

where θ is the slip slope, and ϕ is the friction angle of the material. In Equation (6), $c(y)$ indicates cumulative cohesion at any depth, $W(y)$ is the total weight at any depth and equals to $\int_y^{y_{\text{surf}}} \gamma_m dy$, y_{surf} = 0.85 m is the location of the soil column's surface, and γ_m is the unit total weight of soil. With the help of 1D numerical modeling, as shown in Figure 7, the evolutions of pore water pressure (p^w), pore air pressure (p^a), and volumetric water content (θ^w) can be utilized for slope stability analysis. The evolution of suction can be estimated using $p_c = p^a - p^w$, and the effective degree of saturation can be obtained by $S_e = (\theta^w - \theta_r^w)/(\theta_s^w - \theta_r^w)$.

Let us consider a special condition in which the soil is non-cohesive (c = 0 kPa), the friction angle ϕ = 35°, and the slip slope θ = 20°. In this case, the initial condition of slope stability (FS) was close to 1.92 for the upper layer and close to 1.97 for the lower layer. Figure 9 depicts the evolutions of FS, where the left panel is for open infiltration (Type I) and the right panel is for closed infiltration (Type II). Notably, in both types, the safety factor reduces from ca. 1.92 to ca. 0.78 at the interface of the two layers and from ca. 1.97 to ca. 0.81 at the bottom, but in different patterns.

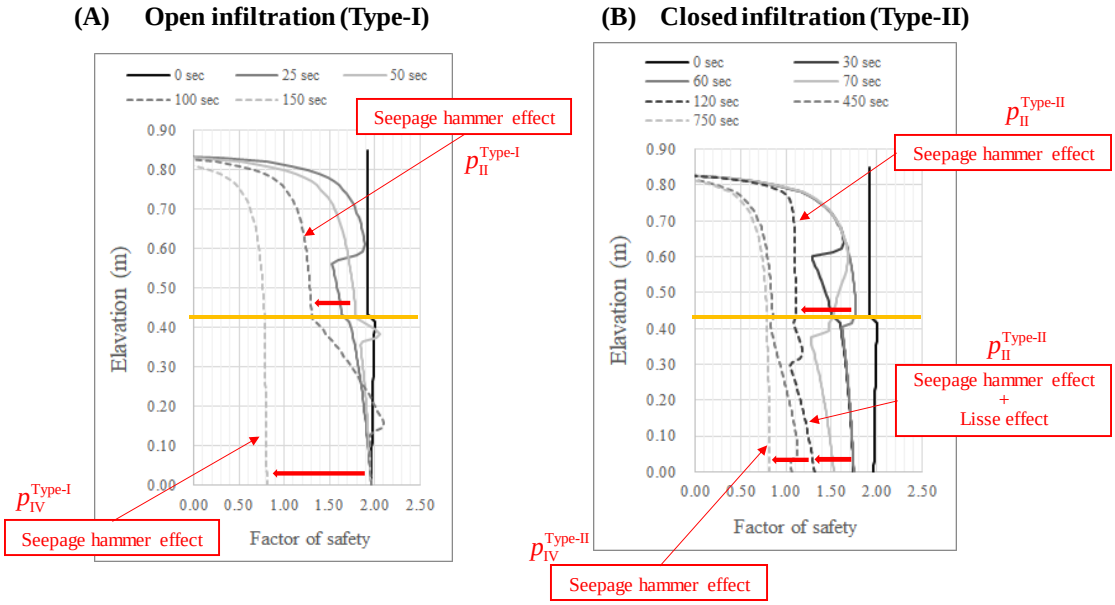

Figure 9. Evolutions of FS: (**A**) open infiltration (Type I); (**B**) closed infiltration (Type II). The yellow line indicates the interface of the two layers; the red arrow indicates the change of the safety factor.

When a constant water head (0.04 m) is mounted at the surface of the soil column, the soil near the ground surface was impacted by the ponding water in both cases, causing a slightly shallow failure (range from y = 0.85 m to y = 0.81 m). For the period P_{I}, 1D numerical modeling reported that the Lisse effect caused rising pore air pressure of the upper layer: ca. 1.0. kPa for open infiltration and ca. 1.5 kPa for closed infiltration, as shown in Figure 7C,F. The Lisse effect caused a decrease in FS at the interface of the two layers from ca. 19.2 to ca. 1.64 for open infiltration (cf. t = 25 s of Figure 9A) and from ca. 19.2 to ca. 1.5 for closed infiltration (cf. t = 30 s of Figure 9B). In the case of closed infiltration, the Lisse effect also caused a decrease in FS at the bottom from ca. 1.97 to ca. 1.74 (cf. t = 30 s of Figure 9B). This study found that the impact of the Lisse effect on the slope stability decreased corresponding to the increase in depth. In the case of open infiltration, the rising pore air pressure dissipated as it passed through the lower layer due to the air permeable boundary condition. Thus, the Lisse effect did not impact the slope stability at the bottom. From the slope stability analysis, in P_{I}, the depth of ponding water and the Lisse effect had a major impact on the slope stability. Accordingly, the potential location of slope failure was higher near the ground surface.

For the period P_{II}, in Section 4.2, the seepage hammer effect was triggered at the interface of the two layers in both cases. Thus, at the interface of the two layers, the *FS* reduced from ca. 1.92 to ca. 1.3 for open infiltration (cf. t = 100 s of Figure 9A) and from ca. 1.92 to ca. 1.1 for closed infiltration (cf. t = 120 s of Figure 9B). This condition has a significant influence on the slope stability. In some steep mountain areas, the slip slope is close to the friction angle, and the slope failure might be induced by the seepage hammer effect easily. Note that the seepage effect can transmit to the bottom of the soil column with the help of the Lisse effect in the case of closed infiltration. At the bottom of closed infiltration, the *FS* reduced from ca. 1.97 to ca. 1.32 (cf. t = 120 s of Figure 9B). An interesting finding is that the cooperation of the seepage hammer effect and the Lisse effect might lead to a slope failure before the wetting front reaches the slip surface. Intense rainfall-induced change in pore air pressure and its impacts on slope stability has been a topic of concern recently [16–18]. This finding could be a potential research topic in the future.

For the period P_{III}, with the help of the column test and 1D numerical modeling, this study found that the wetting front had passed through the interface of the two layers but did not reach the bottom. In both cases, the pore water pressure increased slowly at the interface of the two layers, and the pore air pressure rose gently at the bottom. These slight and gradual changes in pore pressure were not affected by the seepage hammer effect, and the impact on slope stability was relatively minor (cf. Figure 9). From the slope stability analysis, if the difference between the slip slope and the friction angle is large enough, then the slope can remain in an equilibrium state until the wetting front reaches the bottom.

For the period P_{IV}, the importance of the seepage hammer effect can be found from the slope stability analysis. According to the column test and 1D numerical modeling, in the case of open infiltration, the pore water pressure at the bottom reached hydrostatic pressure from a negative value in a short time (ca. 10 s). As a result of this dramatic rise in pore water pressure, the *FS* at the bottom reduced from ca. 1.97 to ca. 0.81 (cf. t = 150 s of Figure 9A). According to the relation between sliding velocity and the change in safety factor [40], in the case of open infiltration, this study inferred that the seepage hammer effect could trigger a fast-moving landslide. In the case of closed infiltration, as shown in Figure 9B, the decreasing value of the safety factor was smaller (from ca. 1.32 to ca. 0.81) and the time consumption for the decrease was longer. In this situation, this study considered that the seepage hammer effect could trigger a slow-moving landslide in closed infiltration only. From the slope stability analysis, the conditions of soil properties (i.e., high air permeability) not only affect the rising speed of pore water pressure but also influence the moving type of landslide potentially.

In summary, first, the slope stability always declines accompanied by the seepage hammer effect. Second, the seepage hammer effect can transmit to a deeper location with the help of the Lisse effect. This study considers the seepage hammer effect an interesting mechanism in the study of fast-moving landslide. Finally, the soil permeability of the water/air has a significant influence on the intensity of the seepage hammer effect and could have a potential influence on moving landslides.

The proposed slope stability analysis is an ideal model for this preliminary study. Furthermore, research on different types of slopes (convex slope, concave slope, . . . etc.) is necessary for the future. Both 2D and 3D numerical modeling should be implemented to investigate general slope problems. For case studies in reality, Take et al. (2004) mentioned that a flow-like landslide in completely decomposed granite fill at Sau-Mau-Ping, Hong Kong, was triggered by heavy rainfall on 18 June 1972 [41]. Padilla et al. (2014) reported that several deep-seated landslides in highly fractured shale fill at Mt. Wanitsuka, Japan, were triggered by Typhoon No. 14 in 2005 [42]. Wu et al. (2013) indicated that a catastrophic landslide in highly fractured shale fill at Hsien-du-shan, Taiwan, was triggered by Typhoon Morakot in 2009 [43]. The aforementioned rainfall-induced landslides, which are composed of highly weathered material, could be potential areas of interest for the practical verification of the seepage hammer effect.

6. Conclusions

This study proposed a new concept of the seepage hammer effect, in which intense rainfall results in a sudden rise in pore water pressure at the interface of multiple layers or impermeable layers. It is a rarely noted phenomenon that has not been completely investigated. In this study, the occurrence mechanism of the seepage hammer effect was researched by applying the column test and a 1D two-phase flow numerical model, and the impact of seepage hammer effect on the slope stability was analyzed by using infinite slope theory. The following investigations and insights were obtained from the results of the column test, the 1D numerical model, and the slope stability analysis.

1. This study proposed a new concept of the seepage hammer effect, which is a mechanism of rainfall-induced abnormal rising pore water pressure. It is triggered when the wetting front reaches the interface of multiple layers or impermeable layers. The increase in pore water pressure is proportional to the developing length of the wetting front. It is different from the Lisse effect and the reverse Wieringermeer effect;
2. The intensity of the seepage hammer effect is affected by the soil properties and geological structure. The effect of the mechanical properties of soil is related to permeability. When the soil layer is highly permeable for water/air and the interstitial air can vent freely, the seepage hammer effect is intense and can trigger a sudden jump in pore water pressure. In the case of open infiltration, the pore water pressure jumped to the total water head of the soil column (0.89 m) in approximately 10 s. In contrast, if the pore air is trapped by infiltrated water and the air venting rate is small, then the seepage hammer effect becomes small and causes a gently rising pore water pressure. In the case of closed infiltration, the pore water pressure took more than 1000 s to reach the total water head of the soil column (0.89 m). In a geological structure that has two layers, an interesting finding is that the seepage hammer effect of the upper layer can be transmitted to the bottom of the lower layer with the help of the Lisse effect;
3. The seepage hammer effect can weaken the slope stability significantly. The decrease in the safety factor is proportional to the intensity of the seepage hammer effect. In the case of open infiltration, the FS can be reduced from ca. 1.97 to ca. 0.81 in approximately 10 s. In contrast, in the case of closed infiltration, the same change of *FS* took more than 1000 s, and with two stages of decay. The relation between the change in the safety factor and the sliding velocity is positive, thus implying that an intense seepage hammer effect could possibly trigger a fast-moving landslide. Thus, the detection of geological structure and soil properties (i.e., interface layer, impermeable layer, hydraulic conductivity, etc.) could be a potential application in the investigation of potential fast-moving landslides;
4. This paper presents preliminary research on the investigation of the seepage hammer effect and its impacts. Some limitations in this study should be improved in future work. For the column test, more sensors should be installed during the experiment to enhance the spatial resolution and measure other physical factors, i.e., volumetric water content and pore air pressure. These data are expected to improve the accuracy of the simulation. For the stability analysis, in reality, different types of slopes (convex slope, concave slope ... etc.) require individual approaches, so 2D and 3D numerical modeling should be implemented to investigate general slope problems. Then, the potential application of the seepage hammer effect in landslide studies can be promoted.

Author Contributions: Conceptualization, C.-L.S., Y.-C.T. and C.-W.L.; methodology, C.-L.S., Y.-C.T. and W.-L.L.; formal analysis, W.-L.L.; manuscript writing, W.-L.L. All authors contributed to improving the paper. All authors have read and agreed to the published version of the manuscript.

Funding: This research received no external funding.

Institutional Review Board Statement: Not applicable.

Informed Consent Statement: Not applicable.

Data Availability Statement: Not applicable.

Conflicts of Interest: The authors declare no conflict of interest.

References

1. Lan, H.; Tian, N.; Li, L.; Wu, Y.; Macciotta, R.; Clague, J.J. Kinematic-based landslide risk management for the Sichuan-Tibet Grid Interconnection Project (STGIP) in China. *Eng. Geol.* **2022**, *308*, 106823. [CrossRef]
2. Lan, H.; Zhang, Y.; Macciotta, R.; Li, L.; Wu, Y.; Bao, H.; Peng, J. The role of discontinuities in the susceptibility, development, and runout of rock avalanches: A review. *Landslides* **2022**, *19*, 1391–1404. [CrossRef]
3. Miao, F.; Zhao, F.; Wu, Y.; Li, L.; Török, Á. Landslide susceptibility mapping in Three Gorges Reservoir area based on GIS and boosting decision tree model. *Stoch. Environ. Res. Risk Assess.* **2023**, 1–21. [CrossRef]
4. Miao, F.; Zhao, F.; Wu, Y.; Li, L.; Xue, Y.; Meng, J. A novel seepage device and ring-shear test on slip zone soils of landslide in the Three Gorges Reservoir area. *Eng. Geol.* **2022**, *307*, 106779. [CrossRef]
5. Rahardjo, H.; Santoso, V.A.; Leong, E.C.; Ng, Y.S.; Hua, C.J. Numerical analyses and monitoring performance of residual soil slopes. *Soils Found.* **2011**, *51*, 471–482. [CrossRef]
6. Touma, J.; Vauclin, M. Experimental and numerical analysis of two-phase infiltration in a partially saturated soil. *Transp. Porous Med.* **1986**, *1*, 27–55. [CrossRef]
7. Weeks, E.P. The Lisse effect revisited. *Groundwater* **2002**, *40*, 652–656. [CrossRef]
8. Lu, N.; Godt, J. Infinite slope stability under steady unsaturated seepage conditions. *Water Resour. Res.* **2008**, *44*, 1–13. [CrossRef]
9. Kuang, X.; Jiao, J.J.; Li, H. Review on airflow in unsaturated zones induced by natural forcings. *Water Resour. Res.* **2013**, *49*, 6137–6165. [CrossRef]
10. Duncan, J.M.; Wright, S.G.; Brandon, T.L. *Soil Strength and Slope Stability*; John Wiley & Sons: Hoboken, NJ, USA, 2014; Available online: http://refhub.elsevier.com/S2214-3912(22)00008-3/h0105 (accessed on 26 March 2020).
11. Siemens, G.A.; Take, W.A.; Peters, S.B. Physical and numerical modeling of infiltration including consideration of the poreair phase. *Can. Geotech. J.* **2014**, *51*, 1475–1487. [CrossRef]
12. Appels, W.M.; Bogaart, P.W.; van der Zee, S.E. Feedbacks between shallow ground-water dynamics and surface topography on runoff generation in flat fields. *Water Resour. Res.* **2017**, *53*, 10336–10353. [CrossRef]
13. Lee, W.L.; Tai, Y.C.; Shieh, C.L.; Miyamoto, K.; Lin, Y.F. Hydro-mechanical response with respect to the air ventilation for water filtration in homogeneous soil. *J. Mt. Sci.* **2019**, *16*, 2562–2576. [CrossRef]
14. Horton, R.E. An approach toward a physical interpretation of infiltration-capacity. *Soil Sci. Soc. Am. J.* **1941**, *5*, 399–417. [CrossRef]
15. Fredlund, D.G.; Rahardjo, H. *Soil Mechanics for Unsaturated Soils*; John Wiley & Sons: Hoboken, NJ, USA, 1993. [CrossRef]
16. Hu, R.; Chen, Y.; Zhou, C. Modeling of coupled deformation, water flow and gas transport in soil slopes subjected to rain infiltration. *Sci. China Technol. Sci.* **2011**, *54*, 2561–2575. [CrossRef]
17. Cho, S.E. Stability analysis of unsaturated soil slopes considering water-air flow caused by rainfall infiltration. *Eng. Geol.* **2016**, *211*, 184–197. [CrossRef]
18. Kang, S.; Kim, B. Effects of coupled hydro-mechanical model considering dual-phase fluid flow on potential for shallow landslides at a regional scale. *Nat. Hazards* **2021**, 1–29. [CrossRef]
19. Rahardjo, H.; Lee, T.T.; Leong, E.C.; Rezaur, R.B. Response of a residual soil slope to rainfall. *Can. Geotech. J.* **2005**, *42*, 340–351. [CrossRef]
20. Hooghoudt, S.B. Waarnemingen van grondwaterstanden voor de landbouw. In *Verslagen Technische Bijeenkomsten*; Scientific Report; Commissie voor hydrologisch onderzoek T.N.O.: Groningen, The Netherlands, 1952; Volume 1–6, pp. 94–110. Available online: https://library.wur.nl/WebQuery/hydrotheek/791175 (accessed on 26 March 2020). (In Dutch)
21. Moriwaki, H.; Inokuchi, T.; Hattanji, T.; Sassa, K.; Ochiai, H.; Wang, G. Failure processes in a full-scale landslide experiment using a rainfall simulator. *Landslides* **2004**, *1*, 277–288. [CrossRef]
22. Waswa, G.W.; Clulow, A.D.; Freese, C.; Le Roux, P.A.L.; Lorentz, S.A. Transient pressure waves in the vadose zone and the rapid water table response. *Vadose Zone J.* **2013**, *12*, 1–18. [CrossRef]
23. Nachabe, M.H.; Sabeh, D. Infiltration in shallow water table environments: Simple two-phase model accounting for air compression and counter flow. *J. Hydrol. Eng.* **2015**, *20*, 04015013–04015016. [CrossRef]
24. Lee, W.L.; Martinelli, M.; Shieh, C.L. An Investigation of Rainfall-Induced Landslides from the Pre-Failure Stage to the Post-Failure Stage Using the Material Point Method. *Front. Earth Sci.* **2021**, *9*, 764393. [CrossRef]
25. Wang, Z.; Feyen, J.; Ritsema, C.J. Susceptibility and predictability of conditions for preferential flow. *Water Resour. Res.* **1998**, *34*, 2169–2182. [CrossRef]
26. Wang, G.; Sassa, K. Pore-pressure generation and movement of rainfall-induced landslides: Effects of grain size and fine-particle content. *Eng. Geol.* **2003**, *69*, 109–125. [CrossRef]
27. Lourenço, S.D.; Sassa, K.; Fukuoka, H. Failure process and hydrologic response of a two layer physical model: Implications for rainfall-induced landslides. *Geomorphology* **2006**, *73*, 115–130. [CrossRef]
28. Gallage, C.; Abeykoon, T.; Uchimura, T. Instrumented model slopes to investigate the effects of slope inclination on rainfall-induced landslides. *Soils Found.* **2021**, *61*, 160–174. [CrossRef]

29. Kitamura, R.; Sako, K. Contribution of "Soils and Foundations" to studies on rain-fall-induced slope failure. *Soils Found.* **2010**, *50*, 955–964. [CrossRef]
30. Srivastava, A.; Babu, G.S.; Haldar, S. Influence of spatial variability of permeability property on steady state seepage flow and slope stability analysis. *Eng. Geol.* **2010**, *110*, 93–101. [CrossRef]
31. Saada, Z.; Maghous, S.; Garnier, D. Stability analysis of rock slopes subjected to seepage forces using the modified Hoek–Brown criterion. *Int. J. Rock Mech. Min. Sci.* **2012**, *55*, 45–54. [CrossRef]
32. SOCIETE NOUVELLE DU LITTORAL. Available online: https://www.standard-sand.com/en/category/products/ (accessed on 26 March 2020).
33. Wyckoff, R.D.; Botset, H.G. The flow of gas-liquid mixtures through unconsolidated sands. *Physics* **1936**, *7*, 325–345. [CrossRef]
34. Goetz, R.O. *Investigation into Using Air in the Permeability Testing of Granular Soils*; Technical Report; The University of Michigan: Ann Arbor, MI, USA, 1971; Available online: https://deepblue.lib.umich.edu/bitstream/handle/2027.42/5147/bac3009.0001.001.pdf?sequence=5 (accessed on 26 March 2020).
35. Van Genuchten, M.T. A closed-form equation for predicting the hydraulic conductivity of unsaturated soils. *Soil Sci. Soc. Am. J.* **1980**, *44*, 892–898. [CrossRef]
36. Mualem, Y. A new model for predicting the hydraulic conductivity of unsaturated porous media. *Water Resour. Res.* **1976**, *12*, 513–522. [CrossRef]
37. Sweijen, T.; Aslannejad, H.; Hassanizadeh, S.M. Capillary pressure–saturation relationships for porous granular materials: Pore morphology method vs. pore unit assembly method. *Adv. Water Resour.* **2017**, *107*, 22–31. [CrossRef]
38. Amankwah, S.K.; Ireson, A.M.; Maulé, C.; Brannen, R.; Mathias, S.A. A Model for the Soil Freezing Characteristic Curve That Represents the Dominant Role of Salt Exclusion. *Water Resour. Res.* **2021**, *57*, e2021WR030070. [CrossRef]
39. Siemens, G.A. Thirty-Ninth Canadian Geotechnical Colloquium: Unsaturated soil mechanics—Bridging the gap between research and practice. *Can. Geotech. J.* **2018**, *55*, 909–927. [CrossRef]
40. Vulliet, L.; Hutter, K. Viscous-type sliding laws for landslides. *Can. Geotech. J.* **1988**, *25*, 467–477. [CrossRef]
41. Take, W.A.; Bolton, M.D.; Wong, P.C.P.; Yeung, F.J. Evaluation of landslide triggering mechanisms in model fill slopes. *Landslides* **2004**, *1*, 173–184. [CrossRef]
42. Padilla, C.; Onda, Y.; Iida, T.; Takahashi, S.; Uchida, T. Characterization of the groundwater response to rainfall on a hillslope with fractured bedrock by creep deformation and its implication for the generation of deep-seated landslides on Mt. Wanitsuka, Kyushu Island. *Geomorphology* **2014**, *204*, 444–458. [CrossRef]
43. Wu, J.H.; Chen, J.H.; Lu, C.W. Investigation of the Hsien-du-Shan rock avalanche caused by typhoon Morakot in 2009 at Kaohsiung county, Taiwan. *Int. J. Rock Mech. Min. Sci.* **2013**, *60*, 148–159. [CrossRef]